

# **Traitement du Signal**

Vol. 42, No. 5, October, 2025, pp. 2693-2704

Journal homepage: http://iieta.org/journals/ts

# A Novel Hybrid Watermarking Scheme for Medical Images Using Dual-Tree Complex Wavelet and 2D Discrete Cosine Transforms



Ali Kouadri <sup>1</sup>, Ali Benziane <sup>1</sup>, Abdelhalim Rabehi <sup>1</sup>, Abdelaziz Rabehi <sup>1</sup>, Amel Ali Alhussan <sup>2</sup>, Doaa Sami Khafaga <sup>2</sup>, El-Sayed M. El-Kenawy <sup>3,4</sup>

- <sup>1</sup>Laboratory of Telecommunication and Smart Systems (LTSS), Faculty of Science and Technology, University of Djelfa, Djelfa 17000, Algeria
- <sup>2</sup> Department of Computer Sciences, College of Computer and Information Sciences, Princess Nourah bint Abdulrahman University, Riyadh 11671, Saudi Arabia
- <sup>3</sup> Department for Communications and Electronics, Delta Higher Institute of Engineering and Technology, Mansoura 35511, Egypt
- <sup>4</sup> Applied Science Research Center, Applied Science Private University, Amman 11937, Jordan

Corresponding Author Email: abdelaziz.rabehi@univ-djelfa.dz

Copyright: ©2025 The authors. This article is published by IIETA and is licensed under the CC BY 4.0 license (http://creativecommons.org/licenses/by/4.0/).

https://doi.org/10.18280/ts.420521

# Received: 2 July 2025 Revised: 22 August 2025 Accepted: 22 September 2025 Available online: 31 October 2025

### Keywords:

watermarking, medical images, DTCWT, DCT2, differential embedding, robustness, imperceptibility, attacks, blind

### **ABSTRACT**

This study introduces a robust watermarking method for medical images using Dual-Tree Complex Wavelet Transform (DTCWT) and 2D Discrete Cosine Transform (DCT2). Binary watermarks are embedded in low-frequency coefficients via differential embedding, leveraging DTCWT's shift-invariance and DCT2's energy compaction for enhanced robustness and imperceptibility. Testing on chest X-ray, CT scan, MRI scan, and ultrasound images demonstrates high visual quality (PSNR = 44.93dB, SSIM = 0.98) while preserving diagnostic integrity. The method achieves perfect watermark recovery (NC = 1.0) against histogram equalization, filtering, and gamma correction, with strong resistance to noise and compression attacks. However, geometric attacks (cropping, rotation) show reduced performance, indicating trade-offs between robustness types. Comparative analysis confirms superior performance over existing methods in most scenarios across all imaging modalities. The blind extraction capability eliminates the need for original images, making it practical for telemedicine applications. This DTCWT-DCT2 hybrid approach offers a promising solution for medical image security during transmission and storage, though geometric attack vulnerabilities require future investigation.

# 1. INTRODUCTION

Telemedicine has transformed healthcare by enhancing accessibility, reducing costs, and enabling remote diagnosis and treatment, especially in situations where in-person consultations are limited or impractical. However, the transmission of medical data over open networks introduces significant security risks, including the potential for unauthorized access, tampering, and data manipulation. Ensuring the confidentiality, integrity, and authenticity of medical images is therefore critical in telemedicine environments. Traditional security measures have limitations, Digital watermarking has emerged as an enhanced protection strategy for medical images, embedding identifying information while maintaining diagnostic quality. Digital watermarking requires balancing robustness imperceptibility. Watermarks must survive processing operations like filtering, compression, and geometric alterations while remaining completely invisible to human observers [1]. These watermarking techniques typically employ either spatial domain or transform domain approaches [2]. Transform-domain techniques, such as Discrete Cosine Transform (DCT) [3], Discrete Wavelet Transform (DWT) [4], and dual-tree complex wavelet transform (DTCWT) [5, 6], have gained significant attention due to their ability to create robust watermarks that withstand common image processing attacks [7]. Research indicates that hybrid approaches combining multiple transformations offer imperceptibility, robustness, and security compared to singletransform methods. DCT watermarking embeds marks in midfrequency coefficients, balancing visual integrity compression resistance by targeting between low-frequency critical) high-frequency (visually and (vulnerable) components. offers excellent spatio-frequency DWT localization, enabling precise watermark placement that leverages human visual system characteristics [5]. Combining DWT with DCT enhances both imperceptibility and robustness against signal processing operations [8]. DWT's limitations include lack of shift invariance (small input shifts cause major coefficient changes) and poor directional selectivity for diagonal features. The Complex Wavelet Transform (CWT) addresses these weaknesses by providing approximate shift invariance and improved directional selectivity with modest redundancy [9]. An enhanced version,

the Dual Tree Complex Wavelet Transform (DTCWT), employs Gabor filters that demonstrate directional selectivity aligned with human visual system characteristics. Studies indicate DTCWT outperforms the combined DWT-DCT approach [10]. The system under consideration therefore integrates DTCWT and DCT properties for more effective watermark embedding and extraction. Several researchers have introduced hybrid approaches in prior studies, including:

Fares et al. [4] developed two blind watermarking methods for telemedicine security: one using DCT with Schur decomposition (targeting mid-frequency components for balanced performance), and another using DWT with Schur (utilizing wavelet properties for enhanced attack resistance). Anand and Singh [11] created a DWT-SVD watermarking method for telehealth that embeds multiple watermarks, applies Hamming code to text watermarks for noise resistance, and uses Chaotic/HyperChaotic encryption with LZW compression for security and efficiency. Verma and Sharma [12] developed a DWT-SVD hybrid watermarking method that embeds patient data in low-frequency DWT sub-bands applying SVD. balancing robustness imperceptibility for telemedicine applications. Khaldi et al. [13] developed a blind watermarking system using RDWT and Schur decomposition, embedding patient data and encrypted photos into mid-frequency coefficients by modifying Eigen values' least significant bits for secure telemedicine. Hebbache et al. [1] proposed a DWT-based blind medical image watermarking approach integrating gradient analysis. The method embeds the watermark into DWT low-frequency (LL) sub-bands, selecting 3×3 block regions based on gradient information. Previous studies have aimed to enhance the security of watermark information using transformation techniques. However, these approaches often suffer from critical limitations, such as an imbalance between imperceptibility and robustness, vulnerability to image processing attacks, and susceptibility to geometric distortions. Addressing these challenges necessitates a refined methodology that simultaneously improves robustness, preserves imperceptibility, and ensures secure embedding for medical imaging applications. This paper proposes a novel and robust hybrid watermarking technique that combines the Dual-Tree Complex Wavelet Transform (DTCWT) and the 2D Discrete Cosine Transform (DCT2). By leveraging the unique advantages of both transforms and employing an innovative differential embedding strategy in optimally selected coefficients, the proposed DTCWT-DCT2 method represents a significant advancement over existing approaches. The technique is purposefully constructed to provide a superior trade-off between imperceptibility and robustness, particularly against geometric attacks. while ensuring blind extraction and heightened security. These features collectively make it a more effective and reliable solution for protecting medical images in telemedicine applications. The structure of this paper is as follows: Section 2 presents the theoretical background of the (DCT) and the DTCWT). The paper is organized as follows: Section 3 details the proposed DTCWT-DCT2 hybrid method and its embedding/extraction processes. Section 4 presents experimental results and comparative performance analysis. Section 5 concludes with key findings.

# 2. THEORY BACKGROUND

### 2.1 Two-dimensional discrete cosine transform (DCT2)

The DCT converts images from spatial to frequency domain

for compression like JPEG. For an  $M \times N$  image, the 2D DCT formula is [14]:

$$T(u,v) = \alpha(u)\alpha(v) \sum_{x=0}^{M-1} \sum_{y=0}^{N-1} f(x,y)$$

$$\cos\left(\frac{(2x+1)u\pi}{2N}\right) \cos\left(\frac{(2y+1)v\pi}{2N}\right)$$
(1)

where, f(x, y) is pixel value, T(u, v) is frequency coefficient, and  $\alpha$  factors are, as defined in reference [14]:

$$\alpha(u) = \begin{cases} \sqrt{\frac{1}{M}} & \text{for } u = 0 \\ \sqrt{\frac{2}{M}} & \text{for } u = 1, 2, ..., M - 1 \end{cases}$$

$$\alpha(v) = \begin{cases} \sqrt{\frac{1}{N}} & \text{for } v = 0 \\ \sqrt{\frac{2}{N}} & \text{for } v = 1, 2, ..., N - 1 \end{cases}$$

$$(2)$$

The inverse DCT (2D-IDCT) transforms frequency data back to spatial domain [14]:

$$f(x,y) = \sum_{u=0}^{M-1} \sum_{v=0}^{N-1} \alpha(u)\alpha(v) T(x,y)$$

$$\cos\left(\frac{(2x+1)u\pi}{2N}\right) \cos\left(\frac{(2y+1)v\pi}{2N}\right)$$
(3)

# 2.2 Dual tree complex wavelet transform

The DTCWT, developed by Kingsbury [10], enhances traditional wavelet transforms by implementing dual parallel filter trees that produce complex coefficients. This approach combines two separates real DWTs with distinct filters (generating real and imaginary components) creating  $2^d$  redundancy for d-dimensional signals [15]. When applied to 2D imagery, the transform yields directionally selective filters at  $\pm 15^\circ$ ,  $\pm 45^\circ$ , and  $\pm 75^\circ$  angles, producing two complex low-frequency and six high-frequency subbands per decomposition level [16] (Figure 1). The low-frequency coefficients can be formulated as:

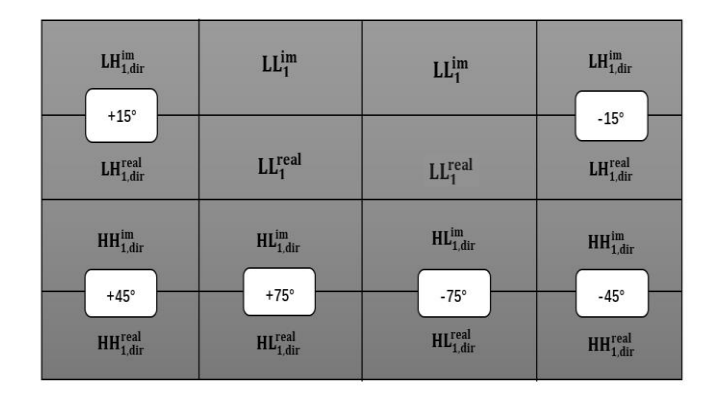


**Figure 1.** DTCWT subband decomposition: Low-frequency and directional high-frequency components

$$y(r, S, i, j) = \Re(y(r, S, i, j)) + j\Im(y(r, S, i, j)), \text{ where } S \in \{S_1, S_2\}$$
(4)

Similarly, the high-frequency components are given by:

$$y(R,\phi,i,j) = \Re(y(R,\phi,i,j)) + j\Im(y(R,\phi,i,j)) \tag{5}$$

where, s,  $\Re(.)$  and  $\Im(.)$  denote the real and imaginary parts, respectively. S<sub>1</sub> and S<sub>2</sub> refer to low-pass sub-bands obtained from the first and second branches of the decomposition. R denotes the decomposition scale, while  $\phi$  specifies the orientation of the sub-band and takes values from the set {-75°, -45°, -15°, +15°, +45°, +75°}. The indices i, j represent the spatial positions within each sub-band and are constrained by: the set  $\{-75^{\circ}, -45^{\circ}, -15^{\circ}, +15^{\circ}, +45^{\circ}, +75^{\circ}\}$ . The indices *i* and j indicate spatial positions within each sub-band and are constrained as:

$$0 \le i \le \frac{H}{2^R} - 1, \qquad 0 \le j \le \frac{W}{2^R} - 1$$
 (6)

This architecture delivers the perfect reconstruction and efficiency of standard DWT while adding shift invariance and directional sensitivity. These properties make DTCWT particularly effective for image processing applications including denoising, segmentation, classification, texture analysis, and digital watermarking, where it provides superior resistance to geometric distortions while maintaining imperceptibility [17].

### 3. SUGGESTED APPROACH

### 3.1 The embedding process

The embedding process is carried out according to the steps outlined in Figure 2 and Algorithm 1:

Apply the 1st level DTCWT to the M×M host image I, extracting low-frequency subbands LL<sub>1</sub> and LL<sub>2</sub>.

Transform subbands using DCT2 generating coefficient matrices  $c_1$  (from  $LL_1$ ) and  $c_2$  (from  $LL_2$ ).

Vectorize coefficient matrices c<sub>1</sub> and c<sub>2</sub> into a 1D arrays  $C_1(n)$  and  $C_2(n)$  (n=1, ..., N=M.M/4).

Convert the 32×32 binary watermark to vector W of length L=1024 and map values from  $\{0, 1\}$  to  $\{-1, +1\}$  for extraction efficiency.

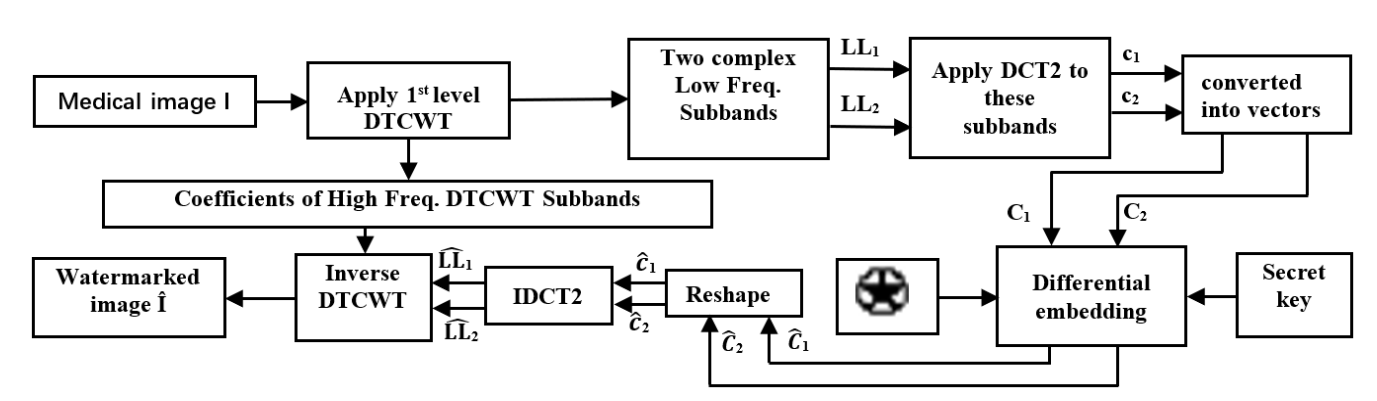


Figure 2. The embedding process of the DTCWT-DCT2 method

# Algorithm 1: Watermarking embedding procedure

function Watermark Embedding

**Parameters:**  $(I, W, \alpha, key)$ 

**Input:** Cover image I; Watermark W; Gain factor (α); encryption key (key).

**Output:** Watermarked Image (I\*).

1:  $LL \leftarrow dddtree2('cplxdt', I, 1, 'dtf3')$ ; // Apply 1stlevel DTCWT to host image I

2:  $LL1 \leftarrow LL. cfs\{2\}(:,:,1,1); \ LL2 \leftarrow LL. c$ , 2, 1); // Extract low-frequency subbands

3:  $c1 \leftarrow dct2(LL1)$ ;  $c2 \leftarrow dct2(LL2)$ ; // Transform subbands

4:  $C1 \leftarrow c1(:)$ ;  $C2 \leftarrow c2(:)$ ; // Vectorize coefficients

5:  $W \leftarrow 2 \times W_b - 1 // \{0,1\} \rightarrow \{-1, +1\}$ 

Generate embedding positions:  $R \leftarrow$ RandPerm(S, x, y)

8: for j=1 to L do

 $9: j' \leftarrow R(j)$ 

10:  $\hat{C}_1(j') \leftarrow 0.5 \times [C_1(j') + C_2(j')] + \alpha \times W(j)$ 11:  $\hat{C}_2(j') \leftarrow 0.5 \times [C_1(j') + C_2(j')] - \alpha \times W(j)$ 

12: end for

13: Reshape coefficients:  $\hat{c}_1 \leftarrow reshape(\hat{C}_1), \hat{c}_2 \leftarrow$ reshape( $\hat{\mathbb{C}}_2$ )

14: Apply inverse transforms: 
$$\widehat{LL}_1 \leftarrow IDCT2(\hat{c}_1), \widehat{LL}_2 \leftarrow IDCT2(\hat{c}_2)$$

Î← Reconstruct watermarked image:  $IDTCWT(\widehat{LL}_1, \widehat{LL}_2, HF\_subbands)$ Return (Î)

Embed the bipolar watermark vector W into the vectors  $\hat{C}_1$ and  $\hat{C}_2$  at specific positions determined by a pre-defined key as follows:

$$\hat{C}_1 = 0.5[C_1 + C_2] + \alpha W$$

$$\hat{C}_2 = 0.5[C_1 + C_2] - \alpha W$$
(7)

where,  $\alpha$  is the gain factor, with j'=R(j), j' indicating embedding positions in  $C_1$  and  $C_2$  bands. These positions are determined by a permutation vector R=RandPerm (S, x, y), where, S initializes the Pseudo-Random Number Generator (PRNG) and x, y mark the high-energy frequency band boundaries. Therefore, the secret key=(S, x, y) prevents unauthorized watermark access.

The modified coefficients  $\hat{C}_1$  and  $\hat{C}_2$  are reshaped into their original matrix forms.

Inverse DCT2 (IDCT2) is applied to obtain the modified subbands  $\widehat{LL}_1$  and  $\widehat{LL}_2$ .

Create the watermarked image  $\hat{I}$  by applying the inverse Dual-Tree Complex Wavelet Transform to the altered approximation coefficients  $\widehat{LL}_1$  and  $\widehat{LL}_2$ , combined with the unchanged Coefficients of High Freq. DTCWT Subbands.

### 3.1.1 Embedding position selection

The choice of embedding positions plays a critical role in balancing imperceptibility and robustness. In the proposed method, the embedding is performed within the DCT2 coefficients of the two low-frequency DTCWT subbands. To ensure that watermark modifications remain visually imperceptible while retaining robustness against attacks, the following strategy is adopted:

- (1) Energy-based selection: After applying DCT2, the energy distribution of coefficients is analyzed. The DC component (first coefficient) is excluded to preserve global luminance. The embedding interval is restricted to higher-energy mid-frequency regions, which are less perceptually sensitive than low-frequency components yet more resilient than fragile high-frequency coefficients.
- (2) Embedding interval definition: A range [x,y] is selected such that:
  - x>0, to avoid DC components;
- $y-x\ge L$ , to ensure sufficient capacity for the watermark length L;
- $y \le N/2$ , where N is the total number of coefficients, ensuring that embedding is confined to stable high-energy regions.
- (3) Optimization strategy: To determine the optimal [x,y], an empirical sensitivity analysis was performed by varying the interval and evaluating imperceptibility (PSNR, SSIM) and

robustness (NC, BCR) metrics. The optimal trade-off was achieved by embedding within mid-frequency coefficients while excluding visually critical and noise-sensitive regions.

(4) Randomized embedding positions: Within the chosen interval, a permutation vector R=RandPerm (S,x,y), initialized by the secret key S, is used to randomize embedding positions. This enhances security by preventing unauthorized detection of the watermark pattern.

This procedure ensures that the embedding process achieves both strong robustness and high imperceptibility while maintaining adaptability across different image sizes and watermark lengths.

### 3.2 The extraction process

The watermark extraction process follows the embedding steps up to Step 5, as shown in Figure 3 and detailed in Algorithm 2. For a watermarked image, Step 4 generates subvectors  $\hat{C}_1$  and  $\hat{C}_2$  Eq. (7). The difference between these vectors is used to recover the watermark W:

$$\Delta C(j) = \widehat{C_1}(j') - \widehat{C_2}(j') = 2\alpha W(j) \tag{8}$$

To extract the estimated watermark sequence  $\widetilde{W}$ , a thresholding operation is applied to the transformed coefficients  $\Delta C(j)$ . This ensures the values conform to the normalized range  $\{-1, +1\}$ . The recovered watermark bits are subsequently derived through the following procedure:

$$\widetilde{W}(j) = \begin{cases} 1 & \text{if } \Delta C(j) \ge 0\\ -1 & \text{otherwise} \end{cases}$$
 (9)

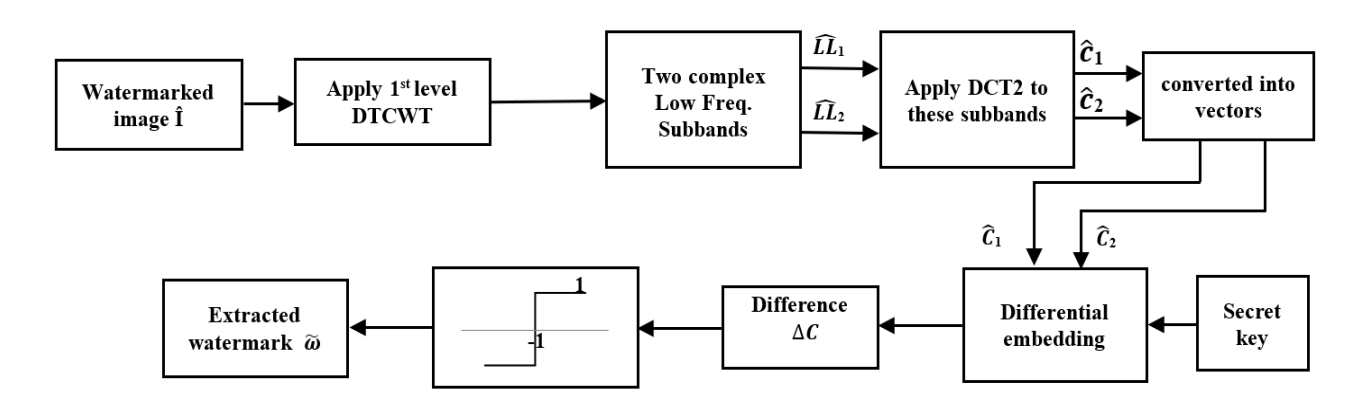


Figure 3. The extraction process of the DTCWT-DCT2 method

# Algorithm 2: Watermarking extracting procedure function Watermark Extraction Parameters: $(\hat{I}, \alpha, L, \text{key})$ Input: Watermarked image $(\hat{I})$ ; Gain factor $(\alpha)$ ; watermark length (L); encryption key (key). Output: Extracted Watermark $(\tilde{\omega})$ . Start 1: Apply 1st-level DTCWT to watermarked image $\hat{I}$ 2: Extract low-frequency subbands: $\widehat{LL}_1$ , $\widehat{LL}_2 \leftarrow$ DTCWT $(\hat{I})$ 3: Transform subbands: $\hat{c}_1 \leftarrow$ DCT2 $(\widehat{LL}_1)$ , $\hat{c}_2 \leftarrow$ DCT2 $(\widehat{LL}_2)$ 4: Vectorize coefficients: $\hat{C}_1 \leftarrow$ vec $(\hat{c}_1)$ , $\hat{C}_2 \leftarrow$ vec $(\hat{c}_2)$ 5: Generate embedding positions: $R \leftarrow$ RandPerm(S, x, y)

6: for j=1 to L do 7:  $i' \leftarrow R(i)$ 

9: if $\Delta C(j) \geq 0$ then 10: $\tilde{\omega}(j) \leftarrow 1$ 11: else 12: $\tilde{\omega}(j) \leftarrow -1$ 13: end if 14: end for 15: Convert extracted bits: $\tilde{\omega}(j) \leftarrow (\tilde{\omega}(j)+1)/2$ // {-1, +1} $\rightarrow$ {0,1} 16: Reshape to image: $\tilde{\omega} \leftarrow$ reshape( $\tilde{\omega}$ , 32×32) 17: return $\tilde{\omega}$ <b>Return</b> ( $\tilde{\omega}$ ) <b>End.</b>	8: $\Delta C(j) \leftarrow \hat{C}_1(j') - \hat{C}_2(j')$
11: else  12:	9: if $\Delta C(j) \ge 0$ then
12:	10:
13: end if 14: end for 15: Convert extracted bits: $\tilde{\omega}(j) \leftarrow (\tilde{\omega}(j)+1)/2 // \{-1, +1\} \rightarrow \{0,1\}$ 16: Reshape to image: $\tilde{\omega} \leftarrow \text{reshape}(\tilde{\omega}, 32 \times 32)$ 17: return $\tilde{\omega}$ Return ( $\tilde{\omega}$ )	11: else
14: end for 15: Convert extracted bits: ω̃(j) ← (ω̃(j)+1)/2 // {-1, +1}→{0,1} 16: Reshape to image: ω̃ ← reshape(ω̃, 32×32) 17: return ω̃ <b>Return</b> (ω̃)	12:
15: Convert extracted bits: $\tilde{\omega}(j)$ ← $(\tilde{\omega}(j)+1)/2$ // {-1, +1}→{0,1} 16: Reshape to image: $\tilde{\omega}$ ←reshape( $\tilde{\omega}$ , 32×32) 17: return $\tilde{\omega}$ <b>Return</b> ( $\tilde{\omega}$ )	13: end if
+1}→{0,1} 16: Reshape to image: ∞̃←reshape(∞̃, 32×32) 17: return ∞̃ Return (∞̃)	14: end for
16: Reshape to image: ã ← reshape(ã, 32×32) 17: return ã Return (ã)	15: Convert extracted bits: $\tilde{\omega}(j) \leftarrow (\tilde{\omega}(j)+1)/2$ // {-1,
17: return $\tilde{\omega}$ Return $(\tilde{\omega})$	$+1\} \rightarrow \{0,1\}$
Return (\tilde{\omega})	16: Reshape to image: $\tilde{\omega}$ ← reshape( $\tilde{\omega}$ , 32×32)
` /	17: return ῶ
End.	Return (\tilde{\alpha})
	End.

#### 4. EXPERIMENTAL SETUP

A comprehensive evaluation of the proposed watermarking scheme was carried out using the publicly accessible COVID-19 chest X-ray database [18]. While CT, MRI, and ultrasound images were obtained from MedPix [19-21]. The evaluation was performed on a Windows 10 system using MATLAB R2023b Update 3, running on an Intel Core i5-6500 CPU (3.2) GHz) with 8GB of RAM. To ensure experimental consistency and mitigate variations arising from dimensional differences. all images were standardized to 512×512 pixels. Figure 4 presents representative examples of these uniformly sized host images from different categories used in the watermarking process. A 32×32 pixel image, representing 1,024 bits of information, was employed as the watermark (Figure 5). This configuration aligns with typical data capacity requirements for securing medical imagery, as documented in the relevant literature [22].

To evaluate the performance of the proposed watermarking method, two primary aspects are considered: imperceptibility and robustness against various attacks. The quality of both the watermarked and restored images is quantitatively assessed using two standard image quality metrics: Peak Signal-to-Noise Ratio (PSNR) and Structural Similarity Index Measure (SSIM). These metrics provide reliable indications of perceptual similarity and distortion levels and are computed according to the formulations described in equations [23]:

$$PSNR(Imo, Imw) = 10 \log_{10} \left( \frac{Mx^2}{MSE(Imo, Imw)} \right) \quad (10)$$

$$MSE(Imo, Imw) = \frac{1}{M^2} \sum_{i,j=1}^{M} (Imo_{i,j} - Imw_{i,j})^2$$
 (11)

$$SSIM(Imo, Imw) = \frac{2\mu_{Imo}\mu_{Imw} + v_1}{\mu_{Imo}^2 + \mu_{Imw}^2 + v_1} \times \frac{2\sigma_{ImoImw} + v_2}{\sigma_{Imo}^2 + \sigma_{Imw}^2 + v_2}$$
(12)









Figure 4. Sample cover medical images

where,

- *Imo*, *Imw*: denote the original and watermarked images.
- M: represent the dimensions of the image.
- Mx: max pixel intensity.
- $\mu_{Imo}$ ,  $\mu_{Imw}$ : represent the mean values of the cover and watermarked images respectively.
- $\sigma_{Imo}^2$ ,  $\sigma_{Imw}^2$ : indicate the variances of the cover and watermarked images respectively.
- $\sigma_{ImoImw}$ : denotes the covariance between the original and the watermarked images.
- $v_1$ ,  $v_2$ : are small positive values significantly less than 1.

SSIM ranges from [0-1], with 1 indicating perfect similarity. Watermark robustness is assessed using normalized cross-correlation (NC) [24] and Bit Correct Rate (BCR) [25].

$$NC(W_{\text{Orig}}, W_{\text{Ext}}) = \frac{\sum_{i=1}^{n} \sum_{j=1}^{n} W_{\text{Orig}_{i,j}} \times W_{\text{Ext}_{i,j}}}{\sqrt{\sum_{i=1}^{n} \sum_{j=1}^{n} W_{\text{Orig}_{i,j}_{i,j}}^{2}} \sqrt{\sum_{i=1}^{n} \sum_{j=1}^{n} W_{\text{Ext}_{i,j}_{i,j}}^{2}}}$$
(13)

where,  $W_{Orig_{i,j}}$  and  $W_{Ext_{i,j}}$  represent the pixel intensities at position (i,j) in the original and extracted watermarks, respectively. NC value of 1 indicates perfect recovery of the watermark. Lower NC values reflect reduced robustness of the watermark against image processing operations or intentional

attacks.

The Bit Correct Ratio (BCR) in Eq. (14) measures the discrepancy between the extracted watermark bits and the originally embedded ones, where ⊕ denotes the (XOR) operation. A BCR of 100% indicates a perfect extraction, meaning no bit errors occurred during the retrieval of the watermark.

$$BCR = \frac{1}{L} \sum_{k=0}^{L-1} \overline{W_{Orig}(k) \oplus W_{Ext}(k)} \times 100\%$$
 (14)



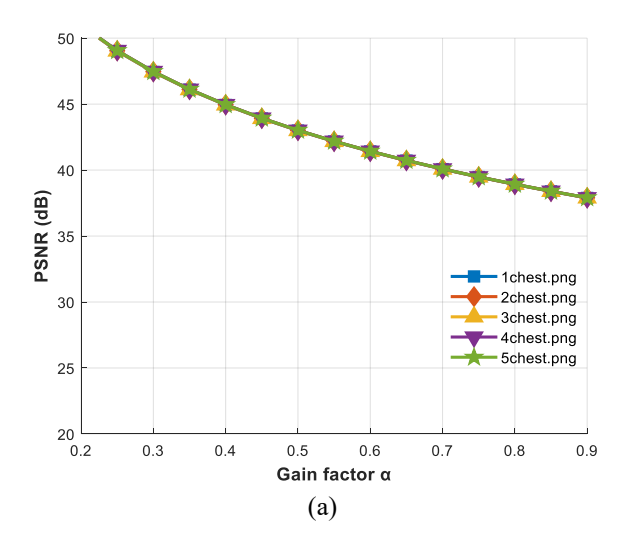
Figure 5. watermark image

### 4.1 Gain factor determination

The parameter  $\alpha$  regulates the trade-off between imperceptibility and robustness: a smaller  $\alpha$  reduces embedding distortion but weakens watermark resilience, whereas a larger  $\alpha$  strengthens robustness at the expense of image quality as shown in Figure 6. To identify the optimal operating point, we evaluated  $\alpha$  over the range [0.1-1.0] in increments of 0.1 and measured the average PSNR, SSIM, NC,

and BCR across the dataset. Two constraints were imposed: (i) imperceptibility thresholds of PSNR  $\geq$ 44dB and SSIM  $\geq$ 0.97 to ensure preservation of diagnostic quality, and (ii) robustness thresholds of NC  $\geq$ 0.95 and BCR  $\geq$ 95% under JPEG compression (Q=50) and Gaussian noise ( $\sigma^2$ =0.01). The results showed that only the interval 0.4-0.5 simultaneously

satisfied both conditions. Lower values of  $\alpha$  (<0.3) failed to ensure sufficient robustness, while higher values (>0.6) caused visible quality degradation. Therefore,  $\alpha$  =0.4 was selected as the default embedding strength, since it provides the best compromise between imperceptibility and robustness in medical image watermarking.



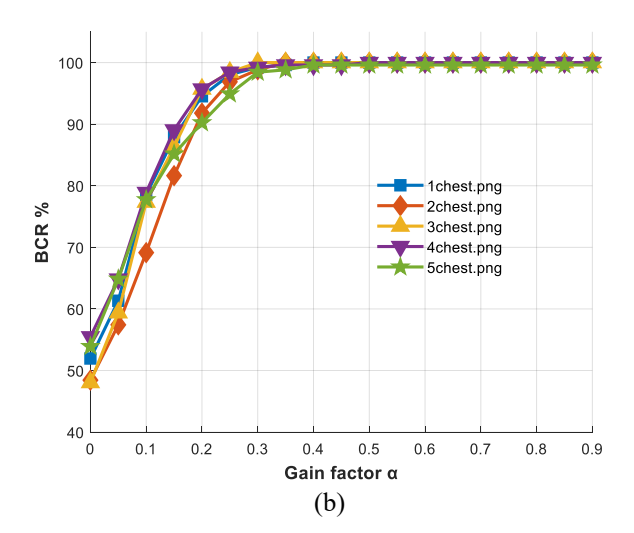
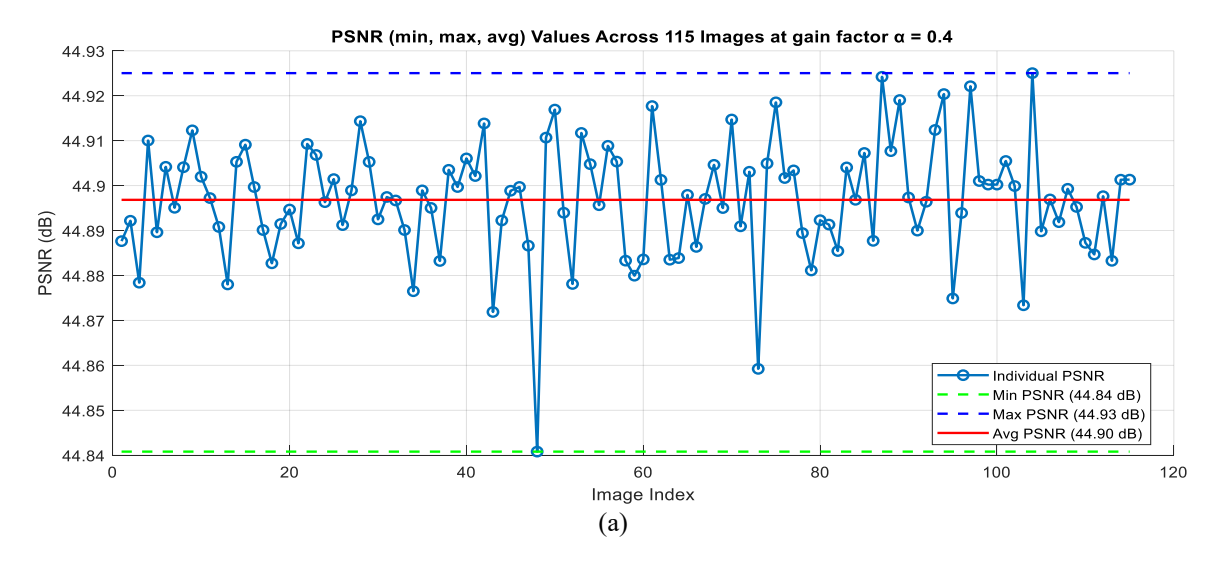


**Figure 6.** PSNR values of the watermarked images in relation to the gain factor  $\alpha$  (a). of the retrieved watermark in relation to the gain factor  $\alpha$  following JPEG lossy compression with quality factor Q=50 (b)

# 4.2 Imperceptibility analysis

The proposed approach is evaluated through visual and numerical analyses to assess imperceptibility and robustness. For privacy preservation, the watermark must remain undetectable. Established thresholds define this requirement: a peak signal-to-noise ratio (PSNR) of ≥29dB indicates high image quality, while values <25dB suggest visible degradation [26]. Similarly, a structural similarity index (SSIM) of ≥0.90 ensures perceptual invisibility [27]. As indicated in Figures 7(a) and 7(b), our watermarking method achieves strong imperceptibility, demonstrated by an average PSNR of 44.90dB -ranging from 44.84 to 44.93dB- across 115 test images. This high PSNR, combined with an SSIM exceeding 0.9827 -ranging from 0.9783 to 0.9867-, confirms that the method introduces modifications indistinguishable to human observers. Figure 8 exemplifies this imperceptibility across diverse medical imaging modalities, showing watermarked images (top row) that maintain excellent visual quality with

PSNR values consistently above 44dB and SSIM values exceeding 0.98, while the corresponding extracted watermarks (bottom row) demonstrate perfect recovery without any attack scenarios. The near-ideal SSIM values further ensure the preservation of critical diagnostic details-a necessity in medical imaging, where even minor alterations risk clinical misinterpretation. In comparative evaluations, as indicated in Table 1, our method demonstrates superior imperceptibility performance across diverse medical imaging modalities. For X-ray images using the COVID-19 Radiography dataset, our approach achieves a PSNR of 44.94 dB, outperforming Saïd et al. [27] (38.74 dB), Fares et al. [4] (44.98 dB), and Hebbache et al. [1] (44.23 dB). Across CT, MRI, and ultrasound images from the MedPix dataset, our method consistently delivers competitive performance with PSNR values of 44.55 dB, 44.53 dB, and 44.54 dB respectively, significantly surpassing Saïd et al. [27] (39.85 dB and 39.38 dB for CT and MRI) while maintaining comparable quality to Hebbache et al. [1] (44.23dB across all modalities).



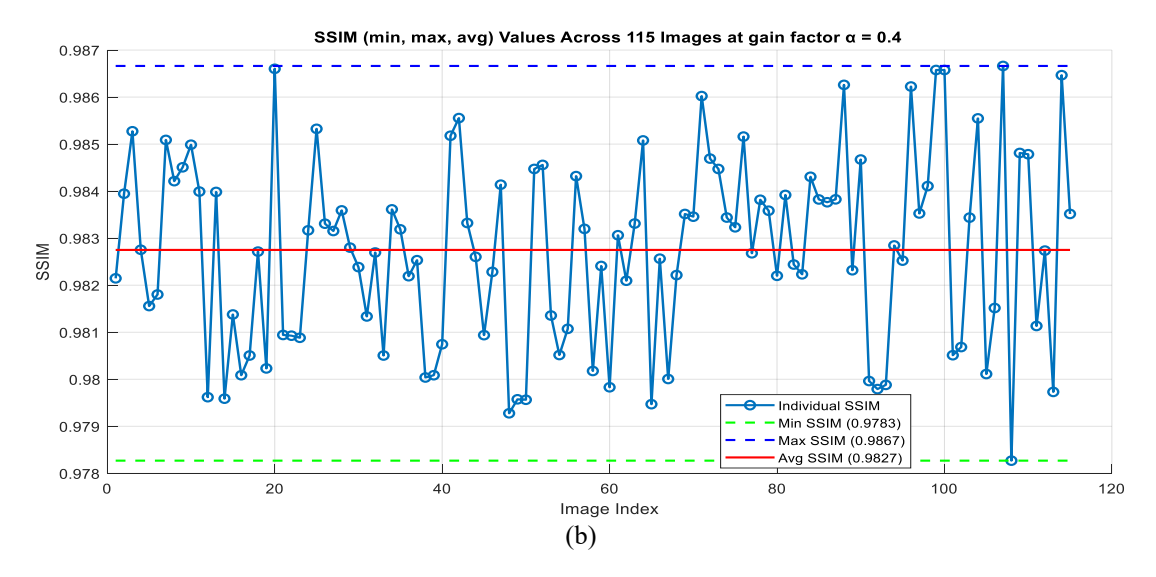


Figure 7. Image quality metrics across 115 test images at gain factor α=0.4: (a) PSNR values and (b) SSIM values

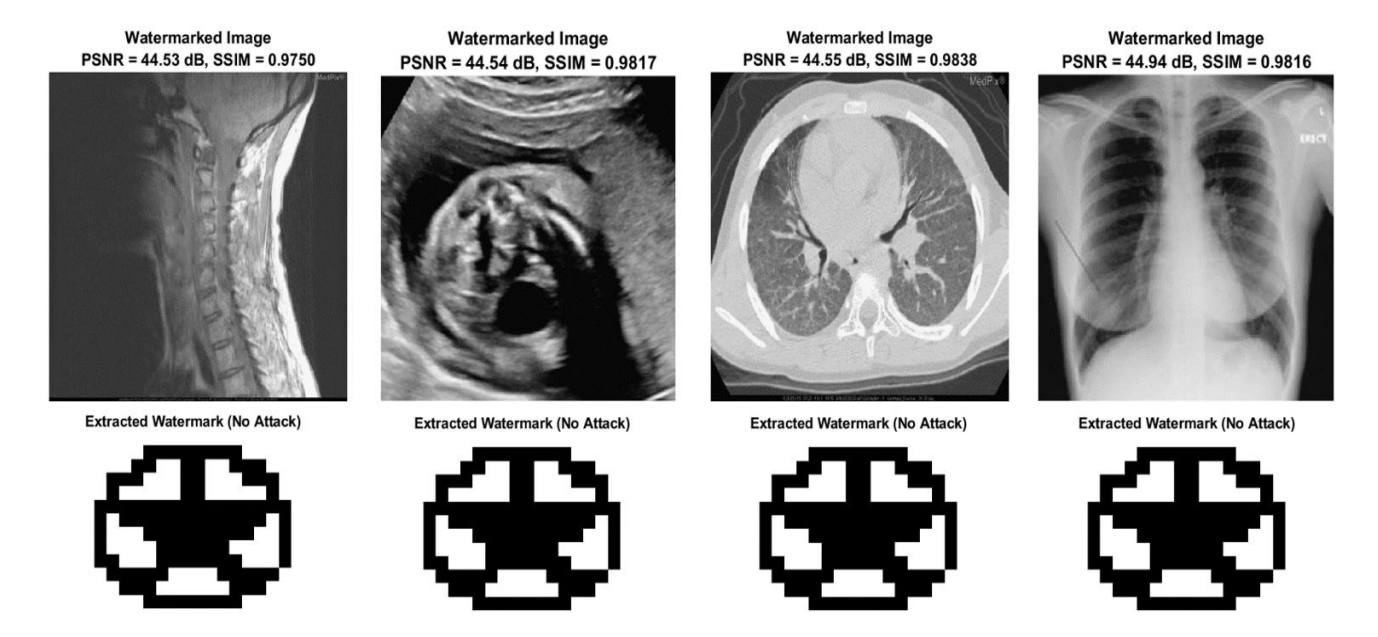


Figure 8. Watermarked images and their extracted watermarks without any attack

**Table 1.** Comparing the imperceptibility of our proposed method with related methods

Test Medical Images	Dataset	Saïd et al. [27]	Fares et al. [4]	Hebbache et al. [1]	Our Method
X-ray image	COVID-19 Radiography	38.74	44.98	44.23	44.94
CT image	MedPix	39.85	N/A	44.23	44.55
MRI image	MedPix	39.38	N/A	44.23	44.53
US image	MedPix	N/A	N/A	44.23	44.54

Table 2. Computational time for embedding and extraction of the proposed watermarking scheme

Input Images	Embedding Time (Sec.)	<b>Extraction Time (Sec.)</b>	Total Time (Sec.)
X-ray image	0.1337	0.0607	0.1944
MRI image	0.1332	0.0614	0.1946
CT scan image	0.1316	0.0635	0.1952
Ultrasound image	0.1358	0.0601	0.1959
The average	0.1336	0.0615	0.1950

# 4.3 Computational complexity and runtime analysis

The computational cost of the proposed DTCWT-DCT2 watermarking scheme arises mainly from the application of the Dual-Tree Complex Wavelet Transform (DTCWT) and the

two-dimensional Discrete Cosine Transform (DCT2). For an input image of size M×M, a single-level DTCWT requires O(M2) operations due to the filtering and downsampling stages, while the DCT2 applied to the two low-frequency subbands (each of size 2M×2M) requires O(M2logM)

operations using fast DCT algorithms. The embedding process involves vectorization and differential modification of coefficients, which is linear in the watermark length L, i.e., O(L). Similarly, the extraction stage mirrors the embedding with comparable complexity. Consequently, the overall complexity of the scheme is dominated by the transform operations and can be expressed as O(M2logM).

To assess practical runtime performance, the method was implemented in MATLAB R2023b on a desktop equipped with an Intel Core i5-6500 CPU (3.2GHz) and 8GB RAM. For medical images of size 512×512 pixels, the average embedding time was 0.1336 seconds, while watermark extraction required 0.0615 seconds (Table 2). Memory consumption remained modest, as only a limited number of transform subbands and coefficient vectors are stored at each stage.

These results demonstrate that the proposed watermarking system is computationally efficient and suitable for near realtime telemedicine applications. In practical deployments, further optimization through compiled languages (e.g., C/C++) or parallelization on GPU hardware would enable faster processing, making the scheme highly applicable for secure and timely medical image transmission.

# 4.4 Assessment of watermarking resilience against attacks

We evaluated the watermarking scheme's robustness across multiple attack categories, with performance metrics detailed in Tables 3 and 4. The scheme achieved perfect resilience (NC=1.0) against histogram equalization, sharpening (0.2), average filtering (3×1), median filtering (3×3), Wiener filtering (3×3), gamma correction (0.5 and 1.5), Gaussian LPF (3×3 with variances 0.05 and 0.05), and speckle noise (variance 0.01). This robustness to intensity transformations and smoothing operations is critical for medical imaging applications where such enhancements are routine.

**Table 3.** NC values and extracted watermarks of the proposed DTCWT-DCT2 based watermarking scheme under different attacks

Attacks	BCR (%)	NC Values	Extracted Watermark
Histogram Equalization	100	1	€
Gaussian noise (0, 0.01)	97.66	0.9793	Carlo Antificanian (1900)
Gaussian noise (0, 0.005)	98.83	0.9932	₩
Sharpening (0.2)	100	1	<b>⊕</b> <b>⊕</b> <b>⊕</b>
Average filtering (3×1)	100	1	₩
Average filtering (3×3)	98.05	0.9831	€
Cropping (25%)	50.78	0.5320	
Cropping (50%)	54.30	0.5841	
Rotation (0.25°)	62.11	0.9829	
Rotation (0.5°)	98.05	0.6689	# <b>%</b> <b>2</b> (43)
JPEG Compression (Q=30)	92.97	0.9388	€
JPEG Compression (Q=40)	99.22	0.9932	
JPEG Compression (Q=50)	100	1	
Salt & Pepper Noise (2 %)	94.53	0.9511	₩
Scaling (50 %)	98.44	0.9864	
Gaussian LPF (3×3), var=0.05	100	1	<b>⊕</b>
Gaussian LPF (3×1), var=0.05	100	1	
Gamma correction (0.5)	100	1	<b>3</b>
Gamma correction (1.5)	100	1	₩
Speckle noise (var=0.01)	100	1	**************************************
Speckle noise (var=0.02)	98.83	0.9898	₩
Median filter (3×3)	100	1	<b>⊕</b>
Wiener filter (3×3)	100	1	<b>⊕</b>

**Table 4.** The extracted watermark after various attacks

Surrounding Crop (35%)	Surrounding Crop (40%)	Surrounding Crop (30%)	JPEG Compression (O=60)	Gaussian Noise (Var =0.01)	
BCR=88.6719%	BCR=84.7656%	BCR=89.0625%	BCR=98.0469%	BCR=95.7031%	(2) BCR=99.2188%
NC=0.8975	NC=0.8651	NC=0.9008	NC=0.9828	NC=0.9622	NC=0.9932

**Table 5.** Comparison of NC values under various attacks with the schemes proposed by Hebbache et al. [1], Fares et al. [4], Khaldi et al. [13] and Saïd et al. [27]

Attacks	NC Values of Our Method	NC Values [11]	NC Values [4]	NC Values [13]	NC Values [27]
Histogram Equalization	1.0000	0.7223	0.8607	0.8945	0.9632
Gaussian noise $(0, 0.01)$	0.9793	0.9803	0.9412	0.9374	0.9743
Sharpening (0.2)	1.0000	0.6506	0.7693	0.8863	N/A
Average filtering $(3\times1)$	1.0000	0.9860	0.8854	N/A	0.9903
Median filtering $(3\times3)$	1.0000	N/A	N/A	N/A	0.9724
Gaussian filtering (3×3)	1.0000	N/A	N/A	N/A	0.9872
Cropping (50%)	0.5841	0.3586	0.6615	0.8831	N/A
Cropping (25%)	0.5320	N/A	N/A	N/A	0.9784
JPEG Compression (Q=30)	0.9388	0.9388	0.9854	N/A	0.9844
JPEG Compression (Q=60)	1.0000	N/A	N/A	N/A	0.9872
Salt & Pepper Noise (2%)	0.9511	0.9251	0.9141	0.9534	N/A
Salt & Pepper Noise (1%)	1.0000	N/A	N/A	N/A	0.9482
Scaling (50%)	0.9864	0.7157	0.7793	0.7411	0.9572

**Table 6.** Comparison of NC values under various attacks with the schemes proposed by Hebbache et al. [1]

Attacks	CT Scan		MRI Scan		Ultrasound	
Attacks	Hebbache et al. [1]	Our Method	[1]	Our Method	[1]	Our Method
Histogram equalization	0.7195	1.0000	0.9433	1.0000	0.8378	1.0000
Gaussian filter [5, 5]	0.9524	1.0000	0.9575	1.0000	0.9199	1.0000
Gaussian filter [3, 3]	0.9833	1.0000	0.9800	1.0000	0.9646	1.0000
Sharpening	0.7264	1.0000	0.9366	1.0000	0.8720	1.0000
Average filtering [3, 3]	0.9678	1.0000	0.9687	1.0000	0.9353	1.0000
Median filter [3, 3]	0.9666	1.0000	0.9174	1.0000	0.9028	1.0000
JPEG compression (Q=60)	0.9970	0.9897	0.9970	0.9532	0.9970	0.9828
Salt and pepper noise (0.01)	0.9691	0.9932	0.9524	1.0000	0.9703	1.0000
Salt and pepper noise (0.02)	0.9278	0.9863	0.8916	0.9899	0.8290	0.9931
Scaling	0.8916	0.9793	0.8916	1.0000	0.8916	1.0000
Gamma correction (1.5)	0.9947	1.0000	0.9819	1.0000	0.9891	1.0000
Resizing $(512 \rightarrow 256 \rightarrow 512)$	0.9787	0.9758	0.9128	1.0000	0.8949	1.0000
Rotation (0.5°)	0.7804	0.5785	0.6314	0.5875	0.6343	0.5979
Surrounding crop (10%)	0.7462	1.0000	0.9950	0.9899	0.9917	1.0000
Speckle noise (0.0001)	0.5142	1.0000	0.5142	1.0000	0.5142	1.0000

The watermark demonstrated excellent noise tolerance across different distortion types. Gaussian noise yielded NC values of 0.9932 (variance 0.005) and 0.9793 (variance 0.01), while salt & pepper noise (2% density) achieved NC=0.9511. Speckle noise with variance 0.02 maintained high performance with NC=0.9898, indicating strong resistance to noise-based attacks commonly encountered during medical image acquisition and transmission. The slight degradation in average filtering performance when kernel size increases from  $3\times1$  (NC=1.0) to  $3\times3$  (NC=0.9831) demonstrates sensitivity to more aggressive smoothing operations.

Compression performance validation showed strong resilience under JPEG standards across all quality factors

tested. JPEG compression achieved NC=0.9388 at Q=30, NC=0.9932 at Q=40, and perfect reconstruction (NC=1.0) at Q=50. Table 4 demonstrates additional compression robustness with JPEG compression at Q=60 yielding BCR=98.0469% and NC=0.9828. Scaling to 50% maintained excellent performance with NC=0.9864, confirming the watermark's stability under resolution changes.

However, the scheme exhibits significant weaknesses against geometric transformations. Rotation attacks demonstrate severe performance degradation with increasing angles, where NC=0.9829 for 0.25° rotation drops dramatically to 0.6689 for 0.5° rotation. This steep decline indicates high sensitivity to angular displacement, likely due

to the spatial domain embedding approach disrupting coefficient relationships during geometric transformation.

Cropping attacks cause the most severe performance degradation across all tested levels. NC values drop substantially to 0.5320 for 25% cropping and 0.5841 for 50% cropping, with corresponding BCR values of 50.78% and 54.30% respectively. Table 4 provides comprehensive evidence showing surrounding crop attacks at 35% (BCR=88.6719%, NC=0.8975), 40% (BCR=84.7656%, NC=0.8651), and 50% (BCR=89.0625%, NC=0.9008) all result in severely compromised watermark integrity. The extracted watermarks display visible corruption patterns and noise artifacts, demonstrating that while partial watermark information survives, complete reconstruction becomes impossible due to direct coefficient loss in cropped regions. The visual comparison in Table 4 clearly illustrates the progressive degradation of watermark quality as cropping severity increases, with the most dramatic deterioration observed in the 40% cropping scenario despite maintaining a relatively high BCR of 84.7656%.

The geometric attack vulnerabilities highlight two primary error sources that limit the scheme's robustness. First, spatial coefficient displacement during rotation disrupts the embedding pattern, causing misalignment between watermark extraction coordinates and actual coefficient locations. Second, direct coefficient loss during cropping removes portions of the embedded watermark data, making complete recovery impossible. The consistently poor performance across all cropping percentages indicates this vulnerability is inherent to the current embedding strategy rather than parameterdependent. Potential improvements to address these implementing rotation-invariant limitations include transforms such as log-polar mapping, deploying redundant embedding across multiple image regions to ensure partial recovery capability, and incorporating error correction coding mechanisms to reconstruct watermark data from surviving coefficients.

As summarized in Tables 5 and 6 compare the proposed DTCWT-DCT2 scheme with recent watermarking methods [1, 4, 13, 27] across diverse attacks and imaging modalities (CT, MRI, Ultrasound). The results show that our approach consistently achieves superior robustness. For example, it attains NC=1.0 under histogram equalization, sharpening, filtering, and gamma correction, where competing methods drop significantly (e.g., NC=0.7223 [1] for histogram equalization and 0.7693 [4] for sharpening). Against Gaussian and salt & pepper noise, our scheme maintains NC above 0.95, outperforming [4, 13]. While geometric attacks such as cropping and small rotations remain challenging (NC≈0.58-0.63), performance under scaling is notably higher (NC=0.9864 vs. 0.7157 [1]). The strong results across modalities highlight the generalization ability of the method. This robustness is attributed to the complementary strengths of DTCWT (shift invariance and directional selectivity) and DCT (energy compaction), which together balance imperceptibility and resilience.

# 4.5 Comparative performance discussion

While the numerical results presented in Tables 2-4 confirm that the proposed scheme achieves higher PSNR, SSIM, and NC values compared to existing methods, it is important to analyze the mechanisms that drive these improvements. The superior robustness of the proposed DTCWT-DCT2 approach

can be attributed to the following factors:

# 4.5.1 Synergistic use of DTCWT and DCT2

- The DTCWT provides approximate shift invariance and strong directional selectivity, which increases resilience against geometric attacks such as scaling and filtering.
- The DCT2 offers strong energy compaction, allowing the watermark to be embedded in stable midfrequency coefficients that are less sensitive to noise and compression.
- Together, these transforms provide complementary strengths, outperforming methods that rely on a single transform (e.g., pure DCT or DWT).

### 4.5.2 Differential embedding strategy

By embedding watermark bits based on the difference between paired coefficients, the method achieves stronger resistance to common intensity operations (e.g., histogram equalization, gamma correction), as relative relationships are preserved even under global modifications.

4.5.3 Optimized embedding in high-energy frequency regions Selecting embedding positions adaptively in high-energy mid-frequency bands balances invisibility and robustness. This explains why the proposed method consistently maintains PSNR >44dB and SSIM >0.95, while also withstanding compression and noise attacks better than competing methods.

# 4.5.4 Blind extraction capability

Unlike some prior methods that require the original image for watermark retrieval, our approach enables blind extraction. This not only increases practicality but also reduces error accumulation when the watermarked image undergoes multiple processing steps.

In summary, the superior performance of the proposed scheme is not only reflected in quantitative metrics but is also rooted in the combined theoretical advantages of the hybrid transform framework, the robustness of the differential embedding mechanism, and the optimized selection of embedding positions.

### 5. CONCLUSION

This study presents a hybrid DTCWT-DCT2 watermarking scheme for medical image security, demonstrating strong performance across multiple imaging modalities. Testing on 2,905 chest X-ray images and additional CT, MRI, and ultrasound datasets confirms high imperceptibility (PSNR=44.93dB, SSIM=0.98) and robust resistance to signal processing attacks, achieving perfect watermark recovery (NC=1.0) against filtering, histogram equalization, and gamma correction.

The method outperforms existing techniques in most attack scenarios through the synergistic combination of DTCWT's shift-invariance and DCT2's energy compaction properties. The differential embedding strategy and blind extraction capability make it particularly suitable for telemedicine applications where original images may be unavailable. The approach can be integrated into clinical workflows as a preprocessing step in PACS systems, enabling direct embedding of patient identification or authentication data into DICOM files without compromising diagnostic quality or

standard compliance.

However, geometric attacks remain a significant limitation. Cropping and rotation attacks substantially degrade performance (NC=0.53-0.67), highlighting the fundamental trade-off between signal processing robustness and geometric invariance in frequency-domain watermarking. This vulnerability limits deployment in scenarios involving extensive image manipulation or format conversion.

Future research should focus on enhancing geometric attack resistance through adaptive embedding, error correction coding, and machine learning-based techniques. Adaptive machine learning is especially promising: CNNs or autoencoders could identify optimal embedding regions to minimize distortion, reinforcement learning could adjust embedding strength dynamically, and GANs could simulate adversarial scenarios to improve robustness. In addition, clinical validation with expert radiologists is needed to assess the impact of subtle distortions on diagnostic reliability. Exploring reversible watermarking and extending the framework to dynamic medical imaging—such as surgical recordings and telemedicine—could further broaden its clinical applicability.

### **ACKNOWLEDGEMENTS**

Princess Nourah bint Abdulrahman University Researchers Supporting Project number (PNURSP2025R754), Princess Nourah bint Abdulrahman University, Riyadh, Saudi Arabia.

### REFERENCES

- [1] Hebbache, K., Aiadi, O., Khaldi, B., Benziane, A. (2025). Blind medical image watermarking based on LBP–DWT for telemedicine applications. Circuits, Systems, and Signal Processing, 44: 4939-4964. https://doi.org/10.1007/s00034-025-03023-x
- [2] Gull, S., Parah, S.A. (2024). Advances in medical image watermarking: A state of the art review. Multimedia Tools and Applications, 83(1): 1407-1447. https://doi.org/10.1007/s11042-023-15396-9
- [3] Li, D., Li, J., Bhatti, U.A., Nawaz, S.A., Liu, J., Chen, Y. W., Cao, L. (2023). Hybrid encrypted watermarking algorithm for medical images based on DCT and improved DarkNet53. Electronics, 12(7): 1554. https://doi.org/10.3390/electronics12071554
- [4] Fares, K., Khaldi, A., Redouane, K., Salah, E. (2021). DCT & DWT based watermarking scheme for medical information security. Biomedical Signal Processing and Control, 66: 102403. https://doi.org/10.1016/j.bspc.2020.102403
- [5] Lebcir, M., Awang, S., Benziane, A. (2024). Robust blind image watermarking scheme using a modified embedding process based on differential method in DTCWT-DCT. Multimedia Tools and Applications, 83(22): 61379-61405. https://doi.org/10.1007/s11042-024-18185-0
- [6] Zebbiche, K., Khelifi, F., Loukhaoukha, K. (2018). Robust additive watermarking in the DTCWT domain based on perceptual masking. Multimedia Tools and Applications, 77(16): 21281-21304. https://doi.org/10.1007/s11042-017-5451-x
- [7] Lebcir, M., Awang, S. (2019). A review on type of attacks

- on fingerprint image and watermarking techniques. IOP Conference Series: Materials Science and Engineering, 551(1): 012071. https://doi.org/10.1088/1757-899X/551/1/012071
- [8] Benoraira, A., Benmahammed, K., Boucenna, N. (2015). Blind image watermarking technique based on differential embedding in DWT and DCT domains. EURASIP Journal on Advances in Signal Processing, 2015(1): 55. https://doi.org/10.1186/s13634-015-0239-5
- [9] Al-Haj, A. (2007). Combined DWT-DCT digital image watermarking. Journal of Computer Science, 3(9): 740-746. https://doi.org/10.3844/jcssp.2007.740.746.
- [10] Kingsbury, N. (1998). The dual-tree complex wavelet transform: A new efficient tool for image restoration and enhancement. In 9th European Signal Processing Conference (EUSIPCO 1998), Rhodes, Greece, pp. 1-4.
- [11] Anand, A., Singh, A.K. (2020). An improved DWT-SVD domain watermarking for medical information security. Computer Communications, 152: 72-80. https://doi.org/10.1016/j.comcom.2020.01.038
- [12] Verma, U., Sharma, N. (2019). Hybrid mode of medical image watermarking to enhance robustness and imperceptibility. International Journal of Innovative Technology and Exploring Engineering (IJITEE), 9(1): 351-359. https://doi.org/10.35940/ijitee.A4126.119119
- [13] Khaldi, A., Redouane, K.M., Bilel, M. (2023). A medical image watermarking system based on redundant wavelets for secure transmission in telemedicine applications. Wireless Personal Communications, 132(2): 823-839. https://doi.org/10.1007/s11277-023-10636-5
- [14] Bouarroudj, R., Souami, F., Bellala, F. Z., Zerrouki, N. (2024). A reversible fragile watermarking technique using Fourier transform and Fibonacci Q-matrix for medical image authentication. Biomedical Signal Processing and Control, 92: 105967. https://doi.org/10.1016/j.bspc.2024.105967
- [15] Selesnick, I.W., Baraniuk, R.G., Kingsbury, N.C. (2005). The dual-tree complex wavelet transform. IEEE Signal Processing Magazine, 22(6): 123-151. https://doi.org/10.1109/MSP.2005.1550194
- [16] Coria, L.E., Pickering, M.R., Nasiopoulos, P., Ward, R.K. (2008). A video watermarking scheme based on the dualtree complex wavelet transform. IEEE Transactions on Information Forensics and Security, 3(3): 466-474. https://doi.org/10.1109/TIFS.2008.927421
- [17] Tawsifur Rhmnan. COVID-19 radiography database. https://www.kaggle.com/datasets/tawsifurrahman/covid 19-radiography-database, accessed on Feb. 27, 2025.
- [18] Lau, J.J., Gayen, S., Ben Abacha, A., Demner-Fushman, D. (2018). A dataset of clinically generated visual questions and answers about radiology images. Scientific Data, 5(1): 180251. https://doi.org/10.1038/sdata.2018.251
- [19] Siragusa, I., Contino, S., Ciura, M.L., Alicata, R., Pirrone, R. (2025). MedPix 2.0: A comprehensive multimodal biomedical data set for advanced ai applications with retrieval augmented generation and knowledge graphs. Data Science and Engineering, 1-17. https://doi.org/10.1007/s41019-025-00297-8
- [20] Henigman, A., Kennedy, B. (2025). MedPix®: Database of medical images, teaching cases, and clinical topics. Medical Reference Services Quarterly, 44(3): 328-333. https://doi.org/10.1080/02763869.2025.2533768
- [21] Yaghmaee, F., Jamzad, M. (2010). Estimating

- watermarking capacity in gray scale images based on image complexity. EURASIP Journal on Advances in Signal Processing, 2010(1): 851920. https://doi.org/10.1155/2010/851920
- [22] Nouioua, N., Seddiki, A., Ghaz, A. (2020). Blind digital watermarking framework based on DTCWT and NSCT for telemedicine application. Traitement du Signal, 37(6): 955-964. https://doi.org/10.18280/ts.370608
- [23] Salama, A.S., Shoitan, R., Abdallah, M.S., Im Cho, Y., Nagm, A.M. (2023). A robust algorithm for digital image copyright protection and tampering detection: Employing DWT, DCT, and blowfish techniques. Traitement du Signal, 40(5): 2019-2027. https://doi.org/10.18280/ts.400520
- [24] Huang, H.C., Chu, S.C., Pan, J.S., Huang, C.Y., Liao, B.Y. (2011). Tabu search based multi-watermarks embedding algorithm with multiple description coding. Information

- Sciences, 181(16): 3379-3396. https://doi.org/10.1016/j.ins.2011.04.007
- [25] Naffouti, S.E., Kricha, A., Sakly, A. (2023). A sophisticated and provably grayscale image watermarking system using DWT-SVD domain. The Visual Computer, 39(9): 4227-4247. https://doi.org/10.1007/s00371-022-02587-y
- [26] Sun, Y., Su, Q., Chen, S., Zhang, X. (2022). A double-color image watermarking algorithm based on quaternion Schur decomposition. Optik, 269: 169899. https://doi.org/10.1016/j.ijleo.2022.169899
- [27] Saïd, B.A., Ali, W., Amine, K., Redouane, K.M., Sahu, A.K. (2025). FDCT-based watermarking for robust and imperceptible medical image protection. Intelligence-Based Medicine, 12: 100280. https://doi.org/10.1016/j.ibmed.2025.100280